Received January 20, 2022, accepted February 7, 2022, date of publication February 14, 2022, date of current version February 23, 2022.
Digital Object Identifier 10.1109/ACCESS.2022.3151356

Low Thermal Conductivity Adhesive as a Key Enabler for Compact, Low-Cost Packaging for Metal-Oxide Gas Sensors

SERGUEI STOUKATCH[1], JEAN-FRANÇOIS FAGNARD[1], FRANCOIS DUPONT[1], PHILIPPE LAURENT[1], MARC DEBLIQUY[2], AND JEAN-MICHEL REDOUTÉ[1], (Senior Member, IEEE)
[1]Microsys Laboratory, Department of Electrical Engineering and Computer Science, University of Liège, 4102 Seraing, Belgium
[2]Service de Science des Matériaux, Faculté Polytechnique, Université de Mons, 7000 Mons, Belgium
Corresponding author: Serguei Stoukatch (serguei.stoukatch@uliege.be)

This work was supported in part by the Microsystème_ULg Microsys Project funded by Wallonia, Belgium; and in part by the Micro+Project co-funded by the European Regional Development Fund (ERDF), Wallonia, Belgium, under Grant 675781-642409.

ABSTRACT Metal-oxide (MOX) gas sensors commonly rely on custom packaging solution. With an ever-increasing demand for MOX gas sensors, there is a clear need for a low cost, compact and high-performance package. During normal operation, MOX sensors are heated up to a temperature in the typical range of 200-300°C. However, the generated heat must not damage or degrade any other part of the assembly. Using 3D finite elements modelling, we developed an optimal package configuration. To thermally insulate the assembly from the heated MOX sensor we have developed in-house a low thermal conductivity xerogel-epoxy composite with 22.7% by weight xerogel and a thermal conductivity of 107.9 mW m^{-1} K^{-1} which is a reduction exceeding 30% compared to commercially available epoxy. Based on the low thermal conductivity xerogel-epoxy composite, we have developed a novel packaging approach that can suit the large family of MOX sensors. The developed alternative packaging solution includes a small number of assembly steps and uses standard processes and techniques. The assembled MOX sensor is low cost and has a low power consumption, while all thermally sensitive assembly parts remain at low temperature during the system's lifetime.

INDEX TERMS Electronics packaging, electronic packaging thermal management, chemical sensors, microassembly, microsensors.

I. INTRODUCTION

With the rapid development of the Internet of Things (IoT) [1] there is an increasing demand for gas sensors used for indoor and outdoor air quality monitoring. Furthermore, gas detection is paramount in consumer, industry, agriculture, environment, safety and security applications [2]. Among gas sensors, the family of metal-oxide (MOX) sensors dominates the sensor market [3]. MOX gas sensors might have different applications but they often have similar operational principles and architecture. Typically, they include a substrate, a heater, a gas sensitive layer, and dedicated packaging [4]. They also have common challenging specifications such as the need for high sensitivity, fast response [2], low power consumption and low cost [5]. MOX sensors are often processed using various technology platforms such as wafer-level fabrication including MEMS [6] and CMOS [7], various ceramic technologies such as screen-printing [8], laser micromachining [9] or a flexible electronic platform like polyimide [10].

Unlike with CMOS dies and MEMS devices, there is as of date no uniform packaging solution to encapsulate MOX sensor dies [11], [12]. Nevertheless, the most common way to package a MOX sensor at a research stage [13] in order to obtain a proof of concept prototype is to use a discrete metal-ceramic or metal package. Such expensive metal-ceramic and metal packages are widely used also for low to medium up to large-scale production. For example, Figaro [14], Bosch [15], SGX [16] and UST [17] offer varieties of MOX gas sensors in metal packages. Renesas [18] offers a large family of gas sensors to detect hydrogen, industrial organic chemicals (including volatile organic compounds) as well as a group of flammable gas sensors, assembled in metal-ceramic

The associate editor coordinating the review of this manuscript and approving it for publication was Ravi Mahajan.

This work is licensed under a Creative Commons Attribution 4.0 License. For more information, see https://creativecommons.org/licenses/by/4.0/

TO-39 packages. MOX sensors are also assembled in plastic packages [9], [17], however it is not clear how the package withstands possible overheating. In [19] authors proposed PCB FR4 based package for the gas sensor, where a micro-heater heats a membrane that reaches temperature of 275°C, meanwhile the sensor remains at lower temperature. The micro-heater is separated from the PCB by an air gap that acts as an insulator and prevents the PCB from the overheating.

Metal and metal-ceramic packages are robust, easy to use and provide a good protection from the environment, such as moisture and contaminants: additionally, they are hardwearing and hence suitable for an extended operation at elevated temperatures [3]. In terms of performance and reliability, they often overcome other types of packaging such a plastic. One of the most important disadvantages of these packages is a high cost which becomes very important for medium and large production scales. The issue of the high cost of metal-ceramic and metal packages is often overlooked at the development and proof of concept stage. Alternatives to these expensive packages are neither obvious nor readily available, and require substantial development: they also may face problems that are difficult to predict.

The paper discusses the advantages and disadvantages of using metal-ceramic TO-5 packages for the assembly of MOX gas sensors. We show the need for alternative packaging and present the challenges to implement it. Next, the development of an adequate packaging solution is described. The alternative package is to replace the expensive TO-5 with a standard PCB. Such transfer is possible by using a specially formulated in-house xerogel-epoxy composite with a low thermal conductivity (107.9 mW m^{-1} K^{-1}). This allows the thermally sensitive PCB to be insulated from the sensor heater without a substantial increase in power consumption.

This paper has the following structure. Section II is dedicated to MOX gas sensors assembled in TO-5 packages, and discusses the advantages and issues related to this package. In section III, we define the requirements for the alternative package. In section IV, we present the numerical model and the results of 3D finite element simulations of the temperature distribution and power consumption of the sensors. In section V, we define an alternative packaging configuration including material selection and packaging geometry. In section VI, we describe the flow of the assembly process. In section VII and VIII, we present the results of the characterization of the device such as thermal mapping and power consumption and compare these experimental results with the corresponding results obtained by numerical modelling. Finally, a conclusion is given in section IX.

II. EXISTING PACKAGING FOR MOX SENSORS

A. SENSOR DIE DESCRIPTION

The sensor exploits the electrical properties of a semiconductor material (a metal oxide) sensitive to the surrounding gases. The electrical conductivity of the sensitive layer is a function of the gas concentration, which is able to be detected thanks to a reversible surface doping caused the gas. The sensor (Fig. 1) consists of an insulating ceramic substrate fitted with a pair of interdigitated gold electrodes (IDE) covered with the sensitive material and a heating element (platinum rectangular track) at the back of the substrate keeping the sensitive layer at its optimal working temperature. The gas sensor is a fully screen-printed double-sided device with 4 electrical terminals (2 for the measurement, 2 for the heater).

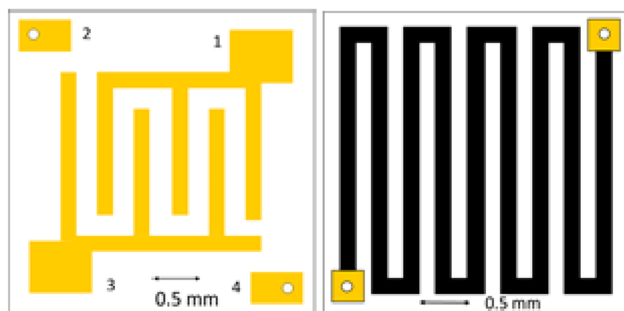

FIGURE 1. Front (left) and rear (right) sides of the sensor die.

In our example, the sensor die is a miniaturized 2.9 × 2.9 mm^2 and 0.5 mm thick alumina ceramic ($Al_2 0_3$) die processed by University of Mons (UMONS) on a 10 × 10 cm^2 ceramic substrate. All materials are deposited by screen-printing. The front and back sides are interconnected by vias.

The resistance of the sensor is changed due to an interaction of the sensing layer with the specific gas. UMONS develops versatile gas sensors [20]–[22] using the described construction and processes these using the same manufacturing platform as the screen-printed technology on ceramic. The final functionality of the sensors is defined by the sensing layer [21]. Indeed, those sensors can be made sensitive to various gases such as H_2 [18], NO_2, ammonia, formaldehyde and isopropanol [21], etc. Typically, the heating temperature of the sensor depends on the sensing layer [20] and ranges from 100°C to 300°C.

B. EXISTING PACKAGES

As a proof of concept, we assembled prototypes of the gas sensor in a TO-5 package. This is a commercially available metal can gold-plated through-hole package, typically used for housing semiconductor devices with a low number of terminals. The TO-5 package is designed in such way that the mounting area acts as a heat sink to facilitate heat transfer from the device to the package and to dissipate it. In this case the die is attached directly to the TO-5 package mounting area using a conventional commercially available non-conductive epoxy Henkel 3609 [23], as depicted in Fig. 2, a bondline is 25-30 μm thick. The sensor heats up to 300°C during normal operation. The heating of the package can cause problems for the integration on a PCB.

Such excessive heating causes unwanted power dissipation and increases the system's overall power consumption. To avoid this, we use another packaging architecture where

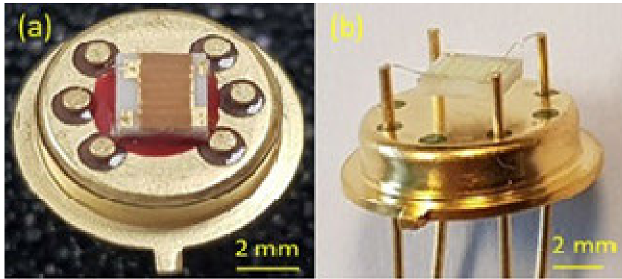

FIGURE 2. Gas sensor directly bonded using an adhesive to the die mounting area of the TO-5 package (a) and the "flying" gas sensor assembled in a TO-5 package (b).

the die has no direct mechanical contact with the TO-5 package. In this construction, the wire bonds also serve as a mechanical support to suspend the sensor die and to provide an air gap between the sensor die and the mounting area of the TO-5 package. This configuration is called the "flying" sensor. Air has a low thermal conductivity at room temperature (0.026 W m^{-1} K^{-1}), and the resulting air gap of 0.8-1 mm acts as a natural thermal insulating medium which prevents heat transfer from the sensor to the package. The assembled and fully functional "flying" sensor is presented in Fig. 2.

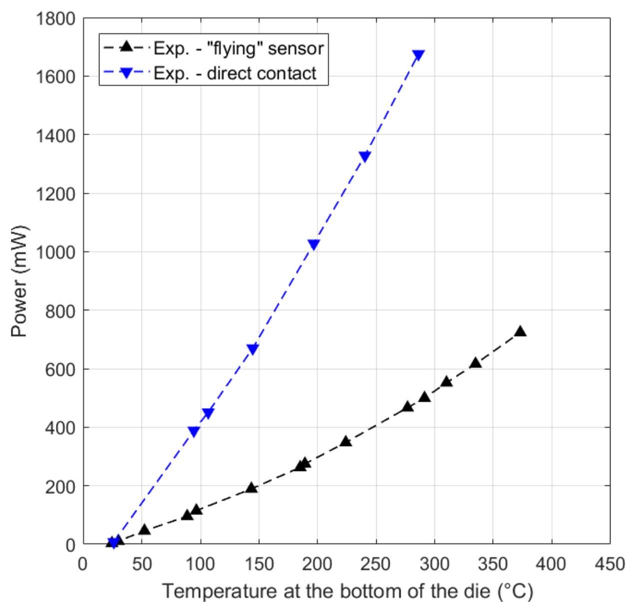

FIGURE 3. Comparison of the power consumption between the "flying" die (black upward triangles) versus the sensor directly bonded on the TO-5 package (blue downward triangles). The details on measurements will be provided in section VIII.

The architecture of the "flying" sensor results in lower power consumption. At 250°C, it is measured to be approximately 3.5 times lower than that of the sensor directly glued on the TO-5 package as illustrated in Fig.3.

The "flying" sensor assembly architecture is conceptually simple, requires a standard package and common direct material as bonding wires, and does not need an adhesive to bond the sensor.

Beside several advantages, among which the most important is the lower power consumption, such a "flying" die packaging solution has several disadvantages. They can be listed as follows: a) the assembly process itself is complex and depends on the skills of the operator, therefore it is difficult to industrialize this task for mass-fabrication, b) the assembly is not robust, c) it is also difficult to control the air gap geometry (such as the width of the gap and the flatness of the plane) between the die and the TO-5 package, d) finally, the TO-5 is expensive, costing up to 7 euro per unit in case of a small scale production.

III. REQUIREMENTS FOR ALTERNATIVE PACKAGING

Based on the initial requirements, the architecture of the alternative package must overcome most of the disadvantages mentioned earlier, in particular the assembly process must be repeatable and allow a full or at least high degree of automation. The resulting assembly must be robust, and the overall cost must be cheaper than when using TO-5. However, the resulting system must keep its functionality and have a power consumption comparable to that of the "flying" die.

The most straightforward way is to mount the sensor die directly onto a conventional electronic carrier such as a printed circuit board (PCB), then electrically interconnect the sensor to the PCB. In the case of a sensor directly mounted on the PCB, there will be, firstly, a significant heat transfer from the sensor to the PCB, secondly, the region under and near the sensor chip will also heat up to 300° C in steady state. The construction of the package shall prevent unnecessary heat dissipation, which will reduce the sensor power consumption and protect the PCB from unnecessary degrading and damaging overheating. The PCB should be made from a common base material that is low cost and able to withstand some thermal exposure. The task is: i) to select a corresponding PCB that can meet the above-mentioned requirements, and ii) to thermally insulate the PCB from the heated sensor. We learned from previous manufacturing tests of "flying" sensors that the insulation through the air gap is effective but difficult to implement in practice, therefore we will first consider a solid thermal insulating material (TIM).

The package requirements and material considerations are translated into an alternative package architecture. Two versions, an electrically conductive adhesive (CA) and a wire bonded (WB) solution have been investigated. In the CA version, an electrical interconnection between the sensor and the PCB is realized by CA tracks that have a large direct contact with assembly parts. In contrast, for the WB version, wire bonds have very small contact area with the terminals on the sensor and the PCB, and the wires pass over other assembly parts without direct contact. Both versions use a PCB (standard or high-performance) as a support or a package body. The PCB design allows to use different TIMs. The schematics of the two versions for the investigated alternative packaging concepts are shown in Fig. 4. The figure includes sectional and top views for the CA and the WB versions.

We have also considered a flip-chip (FC) bonding for mounting the gas sensor on the PCB. However, the conventional FC with tin-silver-copper (Sn-Ag-Cu, known as SAC) alloy solder joint has a melting point of 217–220 °C and is not able to withstand the sensor operational temperature of 250-300°C. A common alternative to SAC FC is CA as an interconnect material, is very similar to the CA version shown above.

In order to verify the proposed alternative packaging architectures and compare the proposed configurations, material selections and geometries, we performed 3D finite elements modelling.

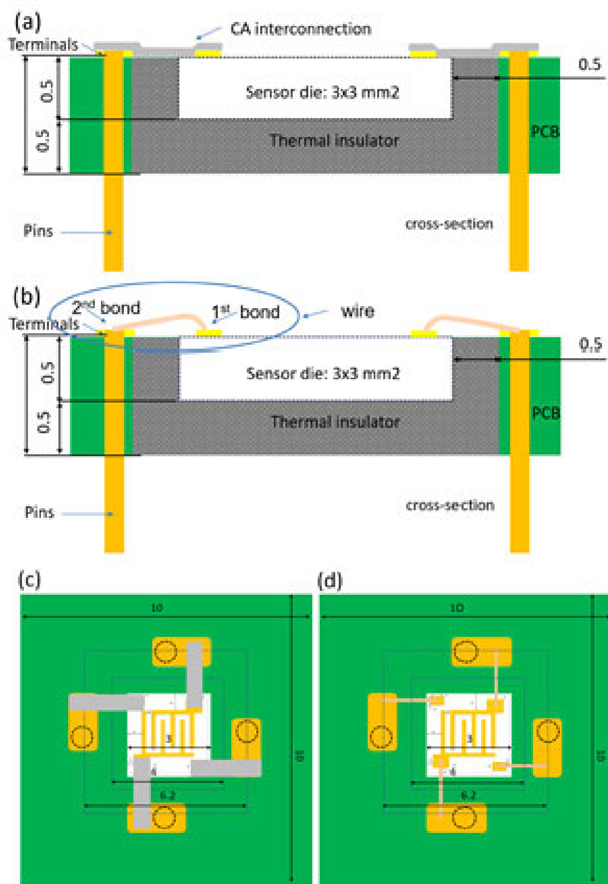

FIGURE 4. Cross-section views (a) of the CA and (b) of the WB versions. Top views (c) of the CA and (d) the WB versions. All dimensions are in mm.

IV. FINITE ELEMENTS MODELLING

A. GEOMETRY AND BOUNDARY CONDITIONS

We designed a 3D finite elements model of the complete packaging solution of the high temperature gas sensor using the open source GetDP software [24]. The model geometry consists of several volumes, i.e. DIE, TIM, PCB, TRACKS, COPPER and AIR. In this section, the modelled parts are named in capital letters to be distinguished from their physical counterparts. The geometry is shown in Fig. 5 and includes the 3 mm × 3 mm × 0.5 mm sensor DIE (in red) of which the lateral and bottom faces are embedded in a 0.5 mm thick thermal insulating material (TIM) layer (in cyan) made of non-conductive adhesive material (i.e. epoxy or xerogel-epoxy composite) which separates the sensor from the supporting PCB (in blue). The dimensions of the PCB are 10 mm × 10 mm × 1 mm. The interconnection TRACKS (in yellow) electrically connect the sensor on the DIE to the mother board, through the COPPER pins (in orange) having a length of 6 mm below and above the PCB and a cross-section of 266 μm × 266 μm. Observe that, in a real sensor, the copper pins would be only on the bottom side while here the COPPER pins are on both sides to fit and allow a more accurate comparison with the experimental setup aiming at thermally separating the chip from the table when measuring the temperature distribution in Section VII and the power consumption in Section VIII.

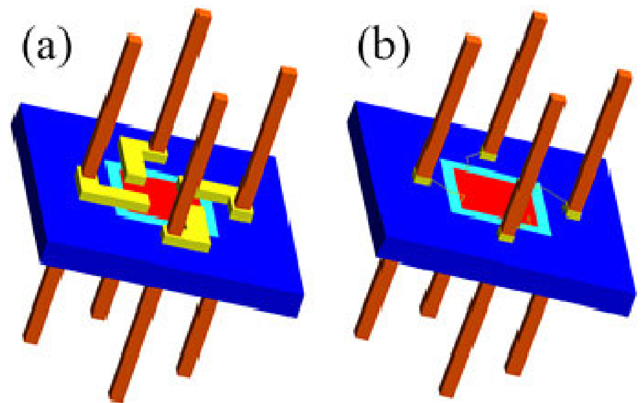

FIGURE 5. 3D model of the studied packaging solution including the sensor die (3 mm × 3 mm × 0.5 mm) in red, the 0.5 mm thick thermal insulating layer (non-conductive adhesive) in cyan, the copper pins for connection to the mother board in orange and the PCB in blue. The interconnection tracks/wires in yellow are respectively (a) conductive adhesive tracks or (b) bonded gold wires.

The interconnection TRACKS consist either (a) of large tracks (in direct contact with the chip) made of conductive adhesive material (for the CA case), and having a cross-section of 800 μm × 400 μm, or (b) of gold wire bonded (for the WB case), the wires having a cross-section of 22.2 μm × 22.2 μm and a lift height of 300 μm. The mesh is refined in order to model even very small gold wires in the WB case. The total number of elements is approximately 2 10^6 tetrahedra.

We aim at comparing the WB case and the CA case by finite element modelling and studying the effects of the thermal conductivity of the PCB and of the TIM layer on the power consumption. This will allow us to select the required materials for improving the sensor's performances and compare the chosen configurations with experimental characterization. The PCB is either a standard FR4 type PCB or a high-performance (larger glass transition temperature) PCB and the TIM layer is either pure epoxy or a xerogel-epoxy composite studied in [25] (specifically, sample 'C3' having a xerogel content of 22.7%wt). We compare the modelling

results obtained for several combinations of material in both interconnection cases. The thermal conductivity of the standard PCB is $k_{\mathrm{PCB-standard}} = 0.3$ W m^{-1} K^{-1} [26] and that of the high-performance PCB is $k_{\mathrm{PCB-high-performance}} = 0.5$ W m^{-1} K^{-1} [27]. For the TIM, the thermal conductivities of both pure epoxy and xerogel-epoxy composite are previously measured and reported in [25], i.e. $k_{\mathrm{TIM-epoxy}} = 0.1679$ W m^{-1} K^{-1} and $k_{\mathrm{TIM-composite}} = 0.1079$ W m^{-1} K^{-1}. The thermal conductivities of all materials used in the 3D model are reported in Table 1.

TABLE 1. Thermal conductivities used in the 3D model.

Material	k (W K^{-1} m^{-1})
DIE (alumina)	25
PCB – standard	0.3
– high-performance	0.5
TIM – composite	0.1079*
– epoxy	0.1679 *
TRACKS – CA case	3.6
– WB case (gold)	317
COPPER	380
AIR	0.04

* The thermal conductivities of TIM are carried out on the same materials used in sections V to VIII and are reported in [25].

Convective and radiative boundary conditions are set on the external surfaces at a given temperature T (in °C) following:

$$F_n = h(T - T_0) \quad (1)$$

$$F_r = h_r((T + 273)^4 - (T_0 + 273)^4) \quad (2)$$

where $h = 20$ W K^{-1} m^{-2}, $T_0 = 20$°C, $h_r = \varepsilon\sigma$ with $\varepsilon = 0.75$ and σ is the Stefan-Boltzmann constant.

B. RESULTS

Figure 6 presents the 3D temperature distribution of the chip in (a) the CA case and (b) the WB case with a high-performance PCB ($k_{\mathrm{PCB}} = 0.5$ W m^{-1} K^{-1}) and where the xerogel-epoxy composite is used as TIM layer ($k_{\mathrm{TIM}} = 0.1079$ W m^{-1} K^{-1}). In each case, the injected power is adjusted to reach a maximum temperature of the DIE at its bottom surface (where the heater is located) $T_{\mathrm{DIE}} = 250$°C which is the operating temperature of the sensor in use.

As all the parts of the chip are shown with the same color scale, we see that the PCB is much colder (darker blue) and the temperature gradient is localized within the TIM layer in the WB case compared to the CA case where we can observe that temperatures on the PCB exceed 150°C. We also notice that the COPPER pins (almost isothermal because of their high thermal conductivity) are colder in the WB case than in the CA case.

The modelling tool allows us to present the 3D temperature distribution of each part of the chip individually. Figure 7 shows this distribution for the DIE, the TIM, and the PCB respectively in (a), (c) and (e) in the CA case and (b), (d) and (f) in the WB case. The simulation parameters are the same as in Fig. 6. By comparing (a) to (b), we observe that more heat is drained out of the DIE through the interconnection tracks in the CA case than through the gold wires in the WB case. By comparing (c) to (d), we observe that the thermal gradient is lower in the CA case (the minimal temperature is 112°C) compared to the WB case where the minimal temperature reaches 87°C, showing that in this particular

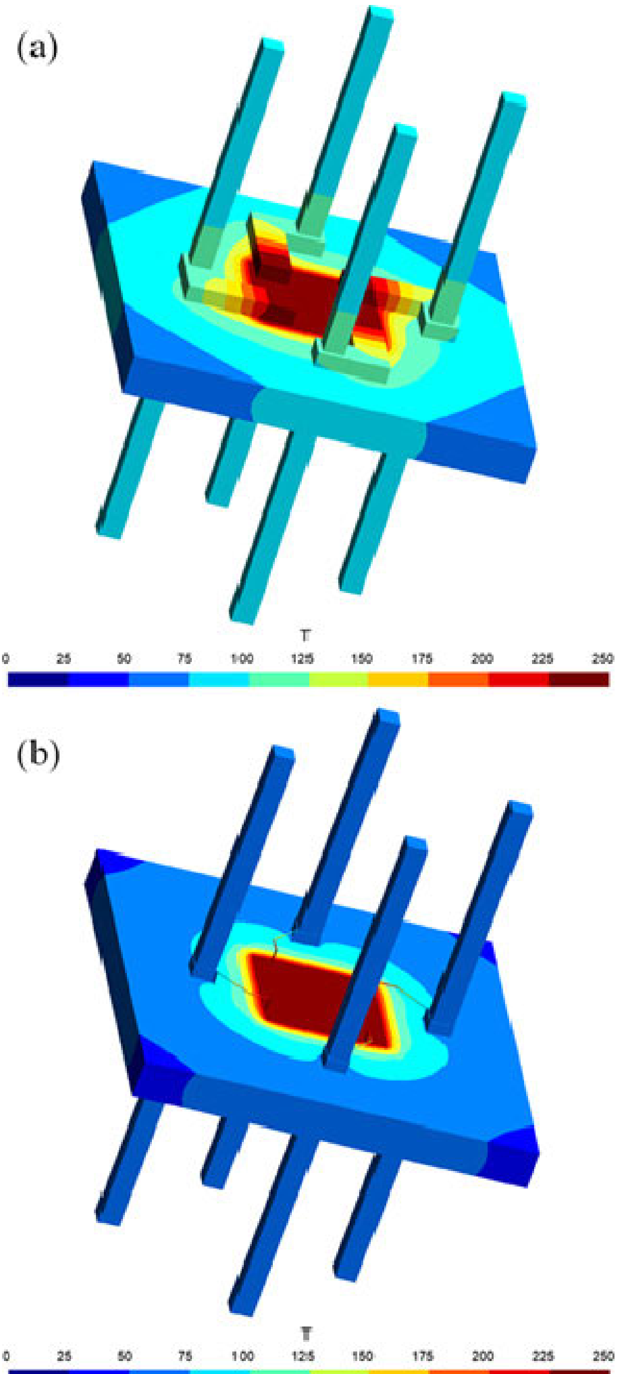

FIGURE 6. 3D temperature distribution of the chip in (a) the CA case and (b) the WB case with a high-performance PCB ($k_{\mathrm{PCB}} = 0.5$ W m^{-1} K^{-1}) and where a xerogel-epoxy composite ($k_{\mathrm{TIM}} = 0.1079$ W m^{-1} K^{-1}) is used as TIM layer. In each case, the injected power is adjusted to reach a maximum temperature $T_{\mathrm{DIE}} = 250$°C.

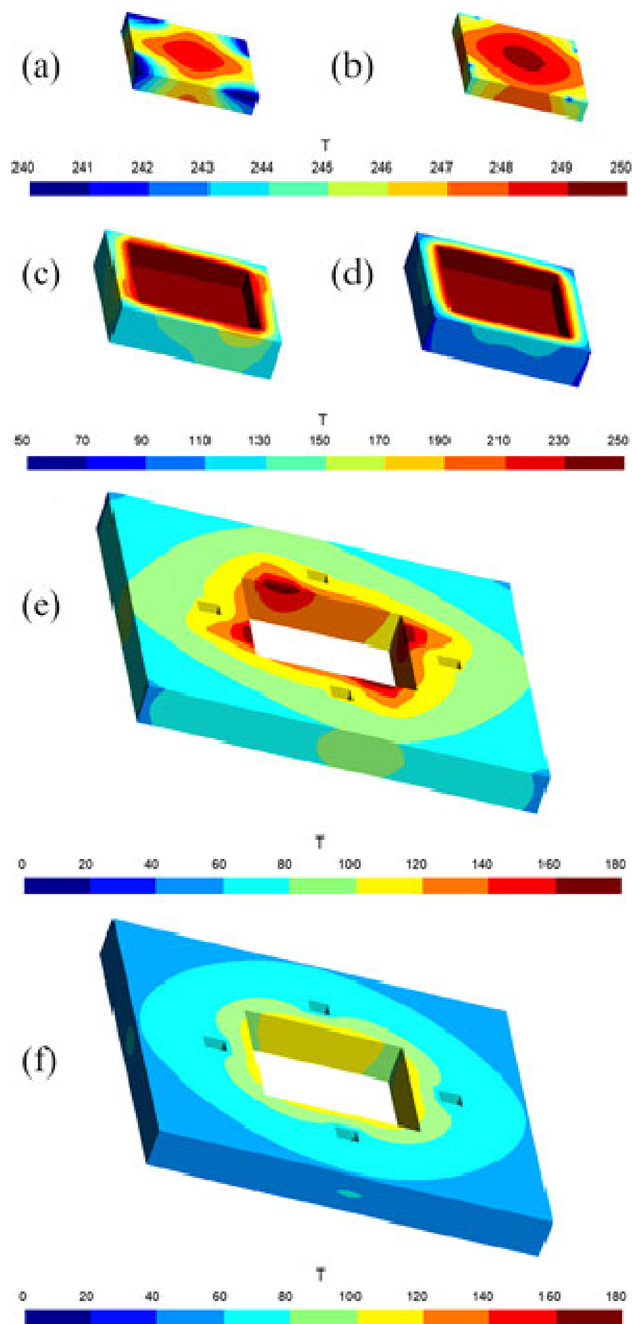

FIGURE 7. **3D temperature distribution of the individual parts of the chip for the DIE, the TIM, and the PCB respectively in (a), (c) and (e) for the CA case and (b), (d) and (f) for the WB case. The simulation parameters are the same as in Fig. 6.**

configuration, the TIM layer presents better performances as thermal insulator between the DIE and the TIM.

Regarding the PCB, the temperature differences between both cases is much easier to describe in this shrunk color scale between 0°C and 180°C compared to Fig. 6. The maximal temperature of 180°C (which corresponds to the glass transition temperature of the high-performance PCB) in the CA case (Fig. 7 (e)) is reached below the interconnection tracks. In the WB case, the temperature profile is more symmetric on the inner lateral surface (at the interface between the PCB and the TIM) and the maximal temperature is only 117°C.

The temperature distribution of the PCB, and in particular its maximal value, can be modelled in the various configurations of TIM and PCB in order to verify that the selected materials can sustain the maximal temperature reached (for a given temperature of the DIE) according to their physical properties and limitations. In Fig. 8, we present the temperature distribution of the PCB in the case of the high-performance PCB (same type as in Figs. 6 and 7) but where pure epoxy replaces the xerogel-epoxy composite for the TIM part. As can be seen, due to the larger thermal conductivity of the TIM part, the temperature of the PCB is slightly larger than in the corresponding case in Fig. 7 (e) and (f) but the effect appears to be less in the CA case (maximal temperature of 184°C instead of 180°C) than in the WB case (maximal temperature of 136°C instead of 117°C). The reason is that the thermal bridges between the DIE and the PCB (i.e. the interconnection tracks) are much less present in the WB case which in return makes the TIM layer very sensitive to property changes such as its increase of thermal conductivity (0.1679 W m^{-1} K^{-1} instead of 0.1079 W m^{-1} K^{-1}).

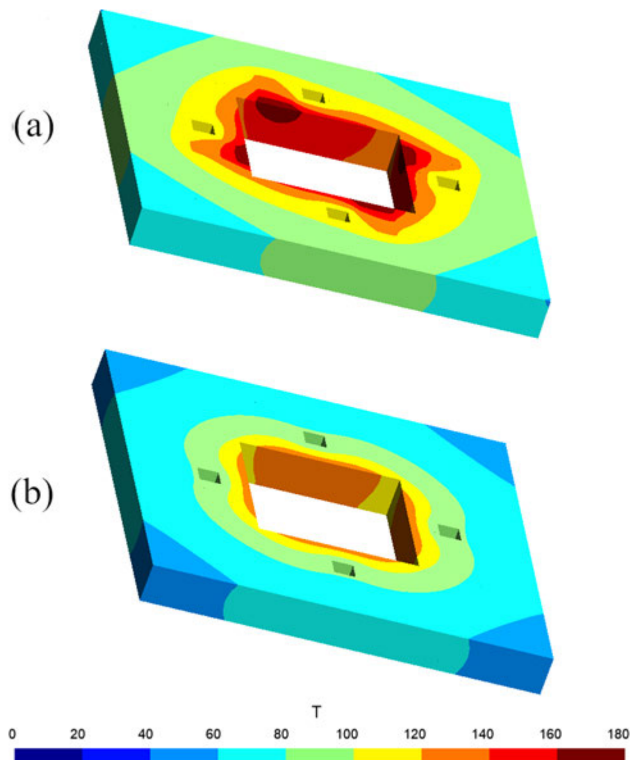

FIGURE 8. **3D temperature distribution of the PCB in (a) the CA case and (b) the WB case with a high-performance PCB and where pure epoxy is used as TIM layer. In each case, the injected power is adjusted to reach a maximum temperature of the DIE at its bottom surface $T_{DIE} = 250$°C. Modelling results are obtained for $k_{PCB} = 0.5$ W m^{-1} K^{-1} (high-performance PCB) and $k_{TIM} = 0.1679$ W m^{-1} K^{-1} (pure epoxy).**

The modelling tool allows us to determine, from the full temperature distribution of the chip, the minimal/maximal temperatures for each part. In particular, for the TIM and the

TABLE 2. Power consumption and temperature ranges.

Case	PCB	TIM	Q for $T_{DIE} = 250°C$ (mW)	TIM T_{min}/T_{max} (°C)	PCB T_{min}/T_{max} (°C)
CA	standard	epoxy	907	125/250	49/187
CA	standard	composite	850	114/250	47/184
CA	high-perf.	epoxy	962	123/250	57/184*
CA	high-perf.	composite	897	112/250	54/180*
WB	standard	epoxy	653	108/250	41/150
WB	standard	composite	570	92/250	38/131
WB	high-perf.	epoxy	703	102/250	47/136
WB	high-perf.	composite	600	87/250	42/117

* Maximum temperatures reached for the high-performance PCB (purple) are only slightly and locally above the glass transition temperature of this PCB.

Red/green color notifies when the maximal temperature is much larger/lower than the glass transition temperature of the PCB.

PCB layers, we can identify the parts that could be affected by an excessively large temperature. Table 2 presents the modelling results obtained for all the studied configurations. In both CA and WB cases, we study (i) two types of PCB (standard and high-performance) and (ii) two types of TIM layer (pure epoxy and xerogel-epoxy composite). For each configuration, the power required to reach a maximum temperature of the DIE equaling 250°C is found through careful iteration.

It can be seen that, for a given couple PCB/TIM, the injected power is between 37 and 49.5% larger when the interconnections between the DIE and the COPPER pins are made through CA tracks in comparison to the corresponding WB case.

In the CA case, when using a xerogel-epoxy composite instead of pure epoxy for the TIM layer, the power is reduced by 6.3 % and 6.8% respectively for a standard PCB and a high-performance PCB. In the WB case, the power reduction rises to 12.7% and 14.7% respectively for a standard PCB and a high-performance PCB. For a given TIM, using a standard PCB instead of a high-performance PCB reduces the injected power between 5 to 7.1% however, depending of the type of PCB, it might not resist the maximal temperature reached at the interface with the TIM layer.

Due to the high thermal conductivity of the DIE, which is more than 2 orders of magnitude larger than the TIM layer, the DIE temperature is almost uniform. In all the cases studied in Table 2, the minimum temperature of the DIE is between 238°C and 241°C when the heater temperature is set at 250°C by injecting the adequate power. Therefore, the min/max temperatures are not listed in Table 2.

Depending on the case, the minimum temperature of the TIM reached at the interface with the PCB (precisely located at each corner on the bottom surface of the chip) ranges between 112°C and 125°C in the CA case while it ranges between 87°C and 108°C in the WB case, showing that a larger temperature gradient is observed across the TIM layer in the latter case. In other words, the insulating character of the TIM layer is enhanced when using wire bonding interconnections compared to using conductive adhesive paste in direct contact with the chip.

Depending on the case, the minimum temperature of the PCB reached at its external corners ranges between 47°C and 57°C in the CA case while it ranges between 38°C and 47°C in the WB case, showing that the PCB is slightly colder in its external area in the latter case. Concerning the maximal temperature, there is a very strong difference in amplitude between the configurations. In the CA case, the maximal temperature ranges between 180°C and 187°C, which makes it impossible to reliably use a standard PCB, while it ranges between 117°C and 150°C in the WB case. When evaluating this data in detail, the maximal temperature exceeds the glass transition temperature of the high-performance PCB as well in the CA case even if only by few °C (180°C – 183°C vs. 180°C). However, this happens only at a very localized area below the CA tracks at the interface with the TIM layer. In the WB case, the maximal temperature of the PCB is several tens of °C below the glass transition temperature of the high-performance PCB (117°C – 136°C vs. 180°C) while for the standard PCB, it is either larger or very close to its glass transition temperature (135°C). For these reasons, the TIM layer should be made of xerogel-epoxy composite material when using a standard PCB and with interconnections made through CA tracks.

Summarizing this modelling section, we choose to realize and characterize the configurations of a high-performance PCB with the xerogel-epoxy composite as TIM layer and comparing experimentally the CA case and the WB case in terms of power consumption.

V. ALTERNATIVE PACKAGING CONCEPT

A. SELECTION OF THE PCB

The PCB must be a low cost, organic-based standard material. FR4 (woven glass–reinforced tetrafunctional epoxy material) is the most common material for designing PCBs and capable to withstanding some thermal exposure. The glass transition temperature T_g is a critical PCB property [28] often used to define an operating temperature, although correlation between both is non-trivial. Following reported recommendations [29], the operating temperature must be minimum of 20°C below T_g. Meanwhile PCB manufacturers list product-specific recommendations, as [30] recommends a safety margin of 20 to 30° C. This margin is 25°C in [31] and [32], and 10 to 20° C in [33]. In our work, we followed a criterion of T_g −25°C to define the operating temperature.

FR4 materials can be classified into two main groups [26]: a standard FR4 type PCB with T_g less than 150°C or a high-performance PCB with T_g above 150°C. Based on thermal modelling results described in Section IV, we considered using a high-performance PCB. To this end, we selected IS410 epoxy laminate and prepreg FR4 [27], 1 mm thick with 35 μm laminated copper finished with 3-5 μm Ni and a 0.05 μm chemically plated Au layer. The PCB has 0.7 mm

diameter vias that are mechanically drilled and plated successively. The coefficient of thermal expansion (CTE) below T_g is 11 ppm/°C, and 13 ppm/°C above T_g [27]. The thermal conductivity of the PCB is 0.5 W m^{-1} K^{-1}. The value of T_g is 180°C and the decomposition temperature is 350°C. Therefore, the PCB must ideally remain at a temperature below 155°C (T_g-25°C) throughout the life cycle of the device: it can, however, withstand short exposures to high temperature above T_g, such as 50 minutes at 260°C.

B. SELECTION OF THE TIM

As indicated previously in [25], there is no commercially available TIM with a thermal conductivity (TC) lower that 0.2 W m^{-1} K^{-1}. In [25], we demonstrated a manufacturing process and presented the characterization of the composite material with thermal conductivity less than 0.2 W m^{-1} K^{-1}. The composite material includes a commercially available epoxy-based adhesive IQ-BOND 2176 (Roartis) and a carbon xerogel (referred to as xerogel in the remainder of the text), an experimental product synthesized at the NCE lab, at the Chemical Engineering Department of University of Liège, Belgium. As reported in [25], we reached a value of 107.9 mW m^{-1} K^{-1} for the xerogel-epoxy composite with 22.7% by weight of xerogel, which is more than 30% less than that for unfilled epoxy. In addition to its low thermal conductivity, the adhesive is a single component which makes it easy to use in manufacturing. The material must also withstand exposure to constant high temperatures of up to 300°C throughout the life cycle of the devices.

C. TGA CHARACTERIZATION OF THE TIM

To check the thermal stability of the material and its resistance to high temperatures, we use thermogravimetric analysis (TGA). TGA measures the mass of a sample over time as the temperature rises with a specified gradient. This method provides information about the physical and chemical phenomena that have occurred in the sample. We performed TGA on the following samples: pure epoxy, pure xerogel powder, and the xerogel-epoxy composite sample (sample C3 in [25]). Sample C3 is 22.7% weight in xerogel content, with a thermal conductivity of 107.9 mW m^{-1} K^{-1} and suitable for dispensing.

TGA analyses were carried out in two different atmospheres: dry air and nitrogen. The normal operating condition of the sensor is ambient atmosphere, meaning that the TGA in air is the main interest of the study in order to identify possible oxidation and combustion phenomena. TGA in an inert atmosphere such as nitrogen makes it possible to identify the thermal decomposition, namely pyrolysis which occurs without the participation of an oxidizing atmosphere. For all the analyses carried out, the temperature ramp was the same and set to 5°C/min. The results of TGA in air and in nitrogen are respectively plotted in Figs. 9 and 10.

The decomposition temperature was defined as an intersection point of the extrapolated baseline of the decomposition

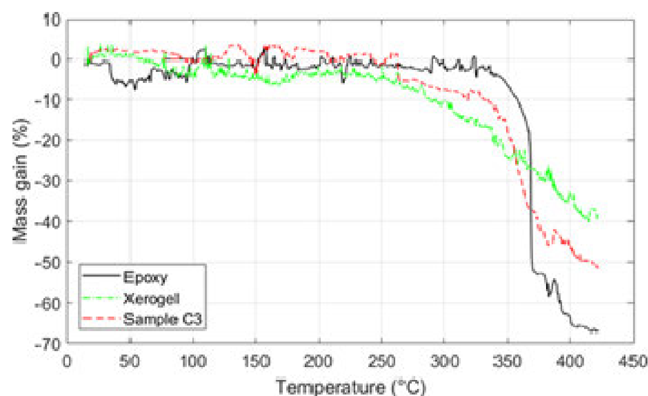

FIGURE 9. TGA curves for pure epoxy, pure xerogel powder, and epoxy-xerogel composite samples obtained in air.

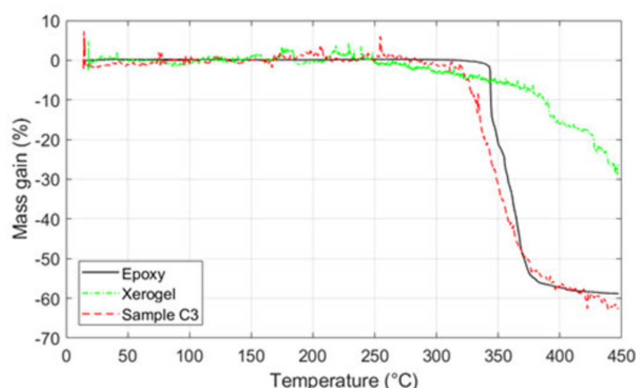

FIGURE 10. TGA curves for pure epoxy, pure xerogel powder, and epoxy-xerogel composite samples obtained in nitrogen.

part of the TGA curve and the mass gain axis (at 0% mass gain).

The decomposition of pure epoxy starts at about 370 °C in air and 340 °C in nitrogen, which can be explained by the fact that in air the surface of the material is oxidized, which forms a thin layer that prevents oxygen from penetrating further into the material. Pure xerogel remains stable up to 270 °C in air and 240°C in nitrogen and exhibits significant mass loss at temperatures exceeding 300°C (3.4% in air and 10.4% in nitrogen). For the epoxy-xerogel composite, the decomposition temperature is 325°C in air and 320°C in nitrogen, which is between that of pure epoxy and of pure xerogel powder. There is no clear difference between processes in air or in nitrogen, which means that pyrolysis is the main mechanism of degradation, and not combustion.

D. ALTERNATIVE PACKAGING CONCEPT ARCHITECTURE

The 3D finite elements modelling enabled us to verify the alternative packaging architecture presented in Fig. 4.

The PCB is 1 mm thick with a micromachined cavity 0.5 mm deep and side dimensions 4 × 4 mm^2 to mount the sensor die. It has 4 electrical terminals to interconnect the sensor die electrically. The electrical terminals are designed to be suitable for wire bonding and using conductive adhesive.

Next to the electrical terminals, there are 4 vias. The vias are 0.7 mm in diameter to accommodate standard 0.65 mm diameter conductive pins. The pins are used to electrically interconnect the package to a system-level board. The pins have the same footprint as the TO-5 package to use an earlier-developed electronic housing and a test bench. The sensor die is thermally insulated from the PCB by the 0.5 mm thick TIM to prevent heat transfer from the die heated to a high temperature of up to 300°C to the carrier PCB.

VI. ASSEMBLY PROCESS FLOW

Assembling the sensors on a PCB is conceptually straightforward and involves well-established processes. The first step is to mount the sensor die on the PCB. For this, the sensor die is placed upside down on a polytetrafluoroethylene (PTFE, commercially known as Teflon) support and aligned in the middle of the corresponding opening in the PCB. The PTFE surface prevents sticking to the support at the end of the assembly operation. The TIM is applied through a dispensing head of 0.25 mm aperture diameter, and is subsequently cured in a convection oven following curing specified schedule [25]. Fig. 11 illustrates the assembly process.

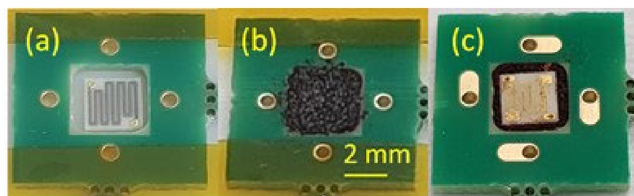

FIGURE 11. Photographs of the sensor mounting on PCB: the sensor die upside down on the PTFE carrier in the middle of the PCB opening (a), TIM dispensed on the PCB (b), cured assembly (face up) detached from the PTFE support (c).

After cooling to room temperature, the assembly is detached from the PTFE support. Then the sensor die is electrically interconnected to the corresponding terminals on the PCB.

As an interconnect adhesive, we chose a previously studied [34] epoxy-based, silver-filled conductive adhesive ABLESTIK 84-1LMIT1 (Henkel). The CA has a low volume resistivity 0.0005 Ω.cm, and a relatively high thermal stability, its weight losses are 0.16% at 300°C. The thermal conductivity is 3.6 W m^{-1} K^{-1}.

We apply the adhesive using a conventional dispensing technique through a 0.2 mm diameter needle aperture. The CA tracks start at the sensor terminals, pass over the TIM and the PCB solder mask, and eventually reach the corresponding PCB terminals. After that, the assembly is cured according to the standard curing schedule recommended by the manufacturer (150°C for 1 h in a convection oven).

For the WB version, we use a thermo-sonic wire bonding technique, carried out on a semi-automatic TPT HB16 wire bonder at 150°C with an Au wire of 25 μm in diameter. The last step of the assembly is to solder 4 conductive pins with a diameter of 0.65 mm. The assembled evaluation CA and WB versions are depicted in Fig. 12. On the evaluation versions, the pins are sticking out of both sides of the PCB to enable top and bottom characterization using a thermal imaging system.

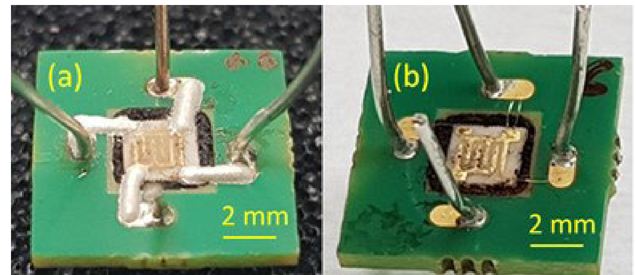

FIGURE 12. Photographs of the front side of the sensor: CA version (a) and WB sensor (b).

The overall cost of the device (including materials and processing) is significantly less than that of the "flying" sensor die in the TO-5 package. The next step is to demonstrate that the assembled sensor meets the required specifications in terms of device performance.

VII. THERMAL CHARACTERIZATION USING IR MICROSCOPE

A thermal characterization is performed on CA and WB sensors using a Sentris IS640 high-resolution thermal imaging system equipped with a 7-14 μm wavelength infrared (IR) vision system.

The system allows us to obtain the temperature distribution across the entire surface of the samples including all its constituent parts (the sensor die, the TIM and the PCB). The experimental set-up is straightforward, it includes heating the sensor until its normal operating temperature and observing the temperature distribution of the assembly using the IR camera. The sample is electrically connected through the pins to the source meter and positioned in front side of the IR camera with a 20 μm objective.

We use a Keithley 2400 sourcemeter to power the heating circuit until it reaches the temperature of 250°C (or 300°C) and we calculate the corresponding power, based on the voltage and the current readings. The sensor is made of 0.5 mm thick alumina ceramic which, due to its high thermal conductivity of 25 W m^{-1} K^{-1}, leads to the temperature on the front face of the sensor die being the same as on the heater.

Because of the different emissivity values due to the presence of various materials in the sensor, the thermal images obtained with the IR camera must be corrected in order to measure the actual temperature of the observed surface. A calibration is performed by heating the assembled sensor to various temperatures with an external heater. Steady state IR images are then taken in order to calibrate the temperature distribution of each part of the assembly. The thermal images, taken for an operating temperature of 250°C, are then corrected and we list the minimum and maximum temperatures of each part in Table 3. The corresponding temperature ranges obtained using 3D FEM modelling are also listed for comparison.

TABLE 3. Temperature ranges at operating temperature of 250°C.

Case	TIM T_{min}/T_{max} (°C)		PCB T_{min}/T_{max} (°C)	
	Modelling	Experimental	Modelling	Experimental
CA	112/250	104/231	54/180	68/151
WB	87/250	92/222	42/117	49/115

The corrected experimental results are in good agreement with the modelling which confirms that the maximum temperature of the PCB in the CA version slightly exceeds T_g of the high-performance PCB (meaning that the sensor can only be used sporadically) while the maximum temperature of the PCB in the WB version of the chip is at least 50°C below the T_g of the high-performance PCB at all times.

VIII. SENSOR POWER CONSUMPTION

In Fig. 13 we plot the results of the power consumption as a function of the sensor temperature measured on the CA and WB sensors. To plot these results, the temperature of the chip was measured using a screen-printed platinum heater which acts as a thermistor. The procedure is the following: a given voltage U_h is applied to the heater and the current I_h is measured after stabilization. The power consumption is $U_h^* I_h$. The resistance of the heater $R_h = U_h/I_h$ increases linearly with the temperature in this temperature range which gives us the temperature of the chip. The temperature coefficient of the platinum heater was checked after a calibration in an oven.

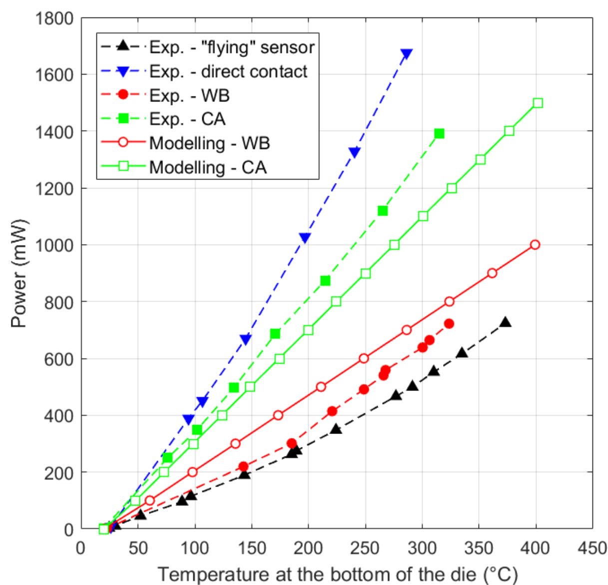

FIGURE 13. Comparison of the power consumption between the "flying" die, the sensor directly bonded on the TO-5 package, the experimental and modelling data for CA and WB sensors.

On the same graph, we include the data of the "flying" sensor and of the sensor directly bonded on the TO-5 package shown in Fig. 3. In addition to the experimental data (dashed lines, solid symbols), we plot the modelling results for the CA and WB sensors (plain lines, open symbols). The power consumption is very high for the CA sensor: at 250°C, it reaches 75% of that measured on the sensor directly bonded to a TO-5 package. This high power consumption is due to the large heat flux transferred from the sensor to PCB though the high thermal conductive CA tracks. For the WB sensor, the power consumption drops to 36% of that measured on the sensor directly bonded to a TO-5 package. The power consumption is only 25% larger than the one measured of the "flying" sensor. Despite the larger thermal conductivity of the gold wires used in the WB case with respect to the thermal conductivity of the CA tracks, the much smaller cross-section of the gold wires drains less heat out of the sensor die. Moreover, the gold wires are not in contact with the TIM layer reducing the heat flux sharing between the interconnections and the TIM. As for the temperature distribution, the power consumption results obtained by modelling are very close to the experimental values. The result that in case of a CA sensor, the modelled results give lower consumption while in the WB case the modelled consumption is larger than what is measured can be explained by the fact that the modelling uses approximations for the physical and geometric properties for both the CA and the WB materials which are uncorrelated. To improve the accuracy of the simulation the physical properties for the CA and WB materials can be experimentally obtained directly on each specific material.

The WB version outperforms the CA version both in terms of power consumption and thermal management.

The final version (WB version) of the MOX gas sensor is presented in Fig. 14.

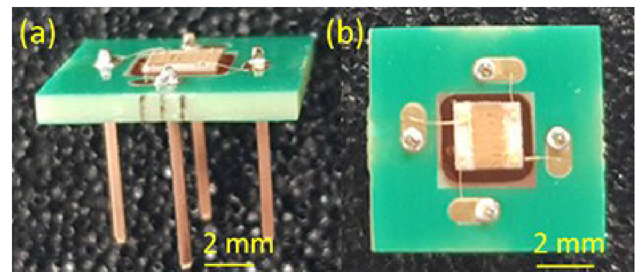

FIGURE 14. Photographs of the sensor: side angle (a) and front side view (b).

IX. CONCLUSION

We have successfully designed and realized an alternative process for packaging MOX gas sensors in a robust, compact and low-cost way. The presented alternative packaging requires a conventional PCB and standard assembly techniques, and replaces the "flying" gas sensor without the need for an expensive TO-5 metal package. The assembled sensor has an acceptable power consumption which is slightly higher than that of the "flying" sensor (+25% at 250°C). For 250°C and 300°C operating temperatures, the maximum temperature of the PCB in steady state remains below the T_g of the PCB (180°C). The PCB was insulated from the sensor heater by an in-house xerogel-epoxy composite which has a low thermal conductivity (107.9 mW m^{-1} K^{-1}). TGA analyses have shown that the decomposition temperature of the xerogel-epoxy composite is 325°C implying that

the xerogel-epoxy TIM is suitable for constant operating temperatures of 250°C and short exposures to temperatures up to 300°C. A 3D finite element model was developed with the GetDP solver for the simulation and prediction of the behavior of the alternative packaging concept at high temperatures. The modelling results show a good correlation with the experimental power consumption measurements and with the temperature distribution obtained by IR imaging.

ACKNOWLEDGMENT

The authors would like to thank Alexandre Megret, Department of Metallurgy, University of Mons for performing the TGA analyses.

REFERENCES

[1] S. Nižetić, P. Šolić, D. López-de-Ipiña González-de-Artaza, and L. Patrono, ''Internet of Things (IoT): Opportunities, issues and challenges towards a smart and sustainable future,'' *J. Cleaner Prod.*, vol. 274, Nov. 2020, Art. no. 122877, doi: 10.1016/j.jclepro.2020.122877.

[2] T. Wasilewski and J. Gębicki, ''Emerging strategies for enhancing detection of explosives by artificial olfaction,'' *Microchem. J.*, vol. 164, May 2021, Art. no. 106025, doi: 10.1016/j.microc.2021.106025.

[3] E. P. Ollé, J. Farré-Lladós, and J. Casals-Terré, ''Advancements in microfabricated gas sensors and microanalytical tools for the sensitive and selective detection of odors,'' *Sensors*, vol. 20, no. 19, p. 5478, Sep. 2020, doi: 10.3390/s20195478.

[4] H. Liu, L. Zhang, K. Li, and O. Tan, ''Microhotplates for metal oxide semiconductor gas sensor applications—Towards the CMOS-MEMS monolithic approach,'' *Micromachines*, vol. 9, no. 11, p. 557, Oct. 2018, doi: 10.3390/mi9110557.

[5] L. Xu, Z. Dai, G. Duan, L. Guo, Y. Wang, H. Zhou, Y. Liu, W. Cai, Y. Wang, and T. Li, ''Micro/nano gas sensors: A new strategy towards *in-situ* wafer-level fabrication of high-performance gas sensing chips,'' *Sci. Rep.*, vol. 5, p. 10507, May 2015, doi: 10.1038/srep10507.

[6] T. Blank, I. Brouk, S. Bar-Lev, G. Amar, E. Meimoun, M. Meltsin, S. Bouscher, M. Vaiana, A. Maierna, M. E. Castagna, G. Bruno, and Y. Nemirovsky, ''Non-imaging digital CMOS-SOI-MEMS uncooled passive infra-red sensing systems,'' *IEEE Sensors J.*, vol. 21, no. 3, pp. 3660–3669, Sep. 2020, doi: 10.1109/JSEN.2020.3022095.

[7] D. Briand, L. Guillot, S. Raible, J. Kappler, and N. F. de Rooij, ''Highly integrated wafer level packaged MOX gas sensors,'' in *Proc. Int. Solid-State Sensors, Actuat. Microsystems Conf.*, Jun. 2007, pp. 2401–2404, doi: 10.1109/SENSOR.2007.4300654.

[8] L. Kulhari, K. Ray, N. Suri, and P. K. Khanna, ''Detection and characterization of CO gas using LTCC micro-hotplates,'' *Sādhanā*, vol. 45, no. 1, pp. 1–6, Dec. 2020, doi: 10.1007/s12046-020-1316-5.

[9] N. N. Samotaev, K. Y. Oblov, and A. V. Ivanova, ''P1SM.8—Technology of rapid prototyping SMD MOX gas sensors,'' in *Proc. IMCS*, 2018, pp. 653–654, doi: 10.5162/imcs2018/p1sm.8.

[10] D. Briand, S. Colin, J. Courbat, S. Raible, J. Kappler, and N. Derooij, ''Integration of MOX gas sensors on polyimide hotplates,'' *Sens. Actuators B, Chem.*, vol. 130, no. 1, pp. 430–435, Mar. 2008, doi: 10.1016/j.snb.2007.09.013.

[11] A. Hierlemann, *Integrated Chemical Microsensor Systems in CMOS Technology*. Berlin, Germany: Springer, 2006.

[12] B. B. Kim and W. Park, ''MEMS packaging,'' in *Encyclopedia Nanotechnology*, B. Bhushan, Ed. Dordrecht, The Netherlands: Springer, 2012, doi: 10.1007/978-90-481-9751-4_319.

[13] M. Graf, A. Gurlo, N. Bârsan, U. Weimar, and A. Hierlemann, ''Microfabricated gas sensor systems with sensitive nanocrystalline metal-oxide films,'' *J. Nanoparticle Res.*, vol. 8, no. 6, pp. 823–839, Dec. 2006, doi: 10.1007/s11051-005-9036-7.

[14] *Figaro*. Accessed: Jan. 20, 2022. [Online]. Available: https://www.figarosensor.com/product/sensor/

[15] *Bosch Sensortec*. Accessed: Jan. 20, 2022. [Online]. Available: https://www.bosch-sensortec.com/products/environmental-sensors/gas-sensors/

[16] *SGX Sensortech*. Accessed: Jan. 20, 2022. [Online]. Available: https://www.sgxsensortech.com/sensor-selector/

[17] *UST*. Accessed: Jan. 20, 2022. [Online]. Available: https://www.umweltsensortechnik.de/en/gas-sensors/mox-gas-sensors-overview.html

[18] *Renesas*. Accessed: Jan. 20, 2022. [Online]. Available: https://www.renesas.com/us/en/products/sensor-products/gas-sensors

[19] R. Prajesh, N. Jain, and A. Agarwal, ''Low cost packaging for gas sensors,'' *Microsyst. Technol.*, vol. 21, no. 10, pp. 2265–2269, Oct. 2015. Accessed: Jan. 20, 2022, doi: 10.1007/s00542-014-2374-6.

[20] Y. Luo, C. Zhang, B. Zheng, X. Geng, and M. Debliquy, ''Hydrogen sensors based on noble metal doped metal-oxide semiconductor: A review,'' *Int. J. Hydrogen Energy*, vol. 42, no. 31, pp. 20386–20397, 2017, doi: 10.1016/j.ijhydene.2017.06.066.

[21] Y. Luo, A. Ly, D. Lahem, C. Zhang, and M. Debliquy, ''A novel low-concentration isopropanol gas sensor based on fe-doped ZnO nanoneedles and its gas sensing mechanism,'' *J. Mater. Sci.*, vol. 56, no. 4, pp. 3230–3245, Feb. 2021, doi: 10.1007/s10853-020-05453-1.

[22] C. Zhang, G. Liu, X. Geng, K. Wu, and M. Debliquy, ''Metal oxide semiconductors with highly concentrated oxygen vacancies for gas sensing materials: A review,'' *Sens. Actuators A, Phys.*, vol. 309, Jul. 2020, Art. no. 112026, doi: 10.1016/j.sna.2020.112026.

[23] *Henkel*. [Online]. Available: https://www.henkel-adhesives.com/be/en/product/electrically-non-conductive-adhesives/loctite_3609.html

[24] P. Dular, C. Geuzaine, F. Henrotte, and W. Legros, ''A general environment for the treatment of discrete problems and its application to the finite element method,'' *IEEE Trans. Magn.*, vol. 34, no. 5, pp. 3395–3398, Sep. 1998, doi: 10.1109/20.717799.

[25] J.-F. Fagnard, S. Stoukatch, P. Laurent, F. Dupont, C. Wolfs, S. D. Lambert, and J.-M. Redoute, ''Preparation and characterization of a thermal insulating carbon xerogel-epoxy composite adhesive for electronics applications,'' *IEEE Trans. Compon., Packag., Manuf. Technol.*, vol. 11, no. 4, pp. 606–615, Apr. 2021, doi: 10.1109/TCPMT.2021.3059478.

[26] C. Coombs and H. Holden, *Printed Circuits Handbook*, 7th ed. New York, NY, USA: McGraw-Hill, 2015.

[27] *Isola Group: PCB Laminates Prepreg*. Accessed: Jan. 20, 2022. [Online]. Available: https://www.isola-group.com/products/IS410

[28] S. Stoukatch, P. Salvo, and M. Hernandez-Silveira, ''Low-temperature microassembly methods and integration techniques for biomedical applications,'' *Wireless Medical Systems and Algorithms. Design and Applications*, P. S. M. Hernandez-Silveira, Ed. Boca Raton, FL, USA: CRC Press, 2016, pp. 21–42.

[29] *Cadence: PCB Design & Analysis*. Accessed: Jan. 20, 2022. [Online]. Available: https://resources.pcb.cadence.com/blog/2020-fr4-maximum-temperature-and-thermal-dissipation

[30] *Leiton*. Accessed: Jan. 20, 2022. [Online]. Available: https://www.leiton.de/pcb-faq-7;53.html

[31] *EuroCircuit*. Accessed: Jan. 20, 2022. [Online]. Available: https://www.eurocircuits.com/blog/how-often-can-you-raise-a-eurocircuits-pcb-to-lead/

[32] *Multi-Circuit*. Accessed: Jan. 20, 2022. [Online]. Available: https://www.eurocircuits.com/blog/how-often-can-you-raise-a-eurocircuits-pcb-to-lead/

[33] *Best-Technology*. Accessed: Jan. 20, 2022. [Online]. Available: https://www.bestpcbs.com/products/high-tg-board.htm

[34] S. Stoukatch, F. Dupont, and M. Kraft, ''Low-temperature packaging methods as a key enablers for microsystems assembly and integration,'' in *Proc. Int. Semiconductor Conf. (CAS)*, Sinaia, Romania, Oct. 2018, pp. 115–118, doi: 10.1109/SMICND.2018.8539847.

SERGUEI STOUKATCH received the Ph.D. degree in electrical engineering from the Moscow Power Engineering Institute—Technical University, Russian Federation, in 1996. He has more than 20 years experience in micro-assembly, packaging and interconnect technology, among them: four years Postdoctoral Researcher with the University of Gent, Belgium, eight years at Interuniversity Microelectronics Centrum (IMEC), Leuven, Belgium, there he followed the career track starting from a Process Engineer to the Assembly Technology Section Head and a Senior Scientist. He is currently a Senior Scientist with the Microsys Laboratory, University of Liège. He holds two patents and author/coauthor more than 80 publications for professional conferences and technical journals. He is specializing in IC, micro-systems, MEMS and biochip packaging, interconnect technology, and 3D integration.

JEAN-FRANÇOIS FAGNARD received the dual Ph.D. degree in engineering sciences from the University of Liège, Belgium, and in applied sciences from the Royal Military Academy, Brussels, Belgium, in 2011.

From 2000 to 2007, he was a Research Engineer and from 2007 to 2008, he was a Teaching Assistant with the Department of Electrical Engineering and Computer Science, University of Liège. From 2008 to 2012, he was a Research Engineer with the Royal Military Academy. In 2013, he was a Research Associate for six months with the University of Cambridge, U.K. He is currently a Research Associate with the Department of Electrical Engineering and Computer Science, University of Liège. His research interests include magnetic and transport properties of high-temperature superconductors for engineering applications (magnetic energy storage, magnetic shielding, and crossed field effect), the properties of materials, such as magnetocaloric materials, colossal magneto-resistive compounds, and the study of flash sintering in ceramic materials and thermal properties of insulating materials.

PHILIPPE LAURENT received the Graduate degree in electromechanical engineering from the University of Liège, Belgium, in 2002, and the Ph.D. degree in measurement and instrumentation, focusing on thermal effects in superconductors.

After, he worked as a Materials and Process Engineer in aeronautics at Safran Aero Booster. Then, he returned to the Microsys Laboratory, University of Liège, as a Research Engineer, in 2010. He is currently doing research in ultra-low-power IoT. In March 2016, he was part of the team that won the prize for the Little Box Challenge, an engineering competition run by Google and the IEEE's Power Electronics Society. In June 2016, he won first prize at the 5G World 2016 Innovation Accelerator, London.

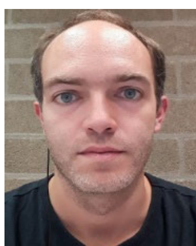

FRANCOIS DUPONT received the M.Sc. degree in electrical and electronics engineering from the University of Liège, Belgium, in 2007.

He subsequently joined the Microsys Laboratory, University of Liège, as a Research Engineer, in 2008. Since then, he has participated in about ten projects whose objectives were the integration/miniaturization of sensor systems. He is currently the Team Leader of the Microsys Laboratory, whose research topics are energy harvesting, connected sensors systems, and advanced packaging. His core competence is the design of miniaturized and ultra-low power electronic circuits.

MARC DEBLIQUY received the Ph.D. degree from the Faculty of Engineering, Mons, Belgium, in 1999. He joined Sochinor Company, in 2000. In 2003, he joined Materia Nova. He was responsible for the research activities in the field of gas sensors. Since October 2008, he has been joining the Material Science Department, Faculty of Engineering, University of Mons and worked as the Team Leader of the Semiconductor and Sensor Group. He was promoted as an Associate Professor, in September 2013. His research interest includes smart coatings for chemical detection. He is also a co-founder of spin off company B-Sens.

JEAN-MICHEL REDOUTÉ (Senior Member, IEEE) received the M.S. degree in electronics from the University College of Antwerp, in 1998, and the M.Eng. degree in electrical engineering from the University of Brussels, in 2001.

In August 2001, he started working at Alcatel Bell, Antwerp, where he was involved in the design of analog microelectronic circuits for telecommunications systems. In January 2005, he joined the University of Leuven as a Ph.D. Research Assistant. In May 2009, he presented his Ph.D. entitled "Design of EMI Resisting Analog Integrated Circuits." In September 2009, he started working with the Berkeley Wireless Research Center, University of California at Berkeley: this research was funded by the Belgian American Educational Foundation (BAEF). In September 2010, he joined Monash University, Melbourne, as a Senior Lecturer. In July 2018, he started working with the University of Liège as an Associate Professor. His research interests include miniaturized and low-power sensor interfaces, robust mixed-signal integrated circuit (IC) design with a high immunity to electromagnetic interference (EMI), biomedical (integrated and non-integrated) circuit design, energy harvesting, and integrated imagers.

Prof. Redouté is an Associate Editor of the IEEE Sensors Journal.